Research Square

Preprints are preliminary reports that have not undergone peer review.
They should not be considered conclusive, used to inform clinical practice,
or referenced by the media as validated information.

Increased-order generalized synchronization in memristive neurons: dissipativity analysis and data-driven control

Dennis Mustafi\'{c}
Friedrich-Alexander-Universität Erlangen-Nürnberg
Marius E. Yamakou
marius.yamakou@fau.de

Friedrich-Alexander-Universität Erlangen-Nürnberg

Research Article

Keywords:

Posted Date: November 24th, 2026

DOI: https://doi.org/10.21203/rs.3.rs-11700453/v1

License: This work is licensed under a Creative Commons Attribution 4.0 International License.
Read Full License

Additional Declarations: No competing interests reported.

Increased-order generalized synchronization in memristive neurons: dissipativity analysis and data-driven control

Dennis Mustafić [1] and Marius E. Yamakou [1,2]

[1]Department of Data Science, Friedrich-Alexander-Universität Erlangen-Nürnberg, Nürnberger Str. 74, Erlangen, 91052, Germany.

[2]Department of Mathematics, Friedrich-Alexander-Universität Erlangen-Nürnberg, Cauer Str. 11, Erlangen, 91058, Germany.

Contributing authors: dennis.mustafic@fau.de; marius.yamakou@fau.de;

Abstract

We investigate increased-order generalized synchronization between four- and five-dimensional memristive Hindmarsh–Rose neurons, focusing on the selection and stabilization of the synchronization map. An analytical construction combines a prescribed nonlinear map with adaptive control, retaining the memristive switching contribution explicitly in the error dynamics. Lyapunov analysis establishes asymptotic synchronization under uniform strict dissipativity and yields a switching-independent decrease estimate outside an explicit error neighborhood. Numerical simulations exhibit error decay beyond the sufficient convergence conditions. A complementary data-driven construction uses next-generation reservoir computing to learn predictors from uncoupled full-state trajectories and an affine synchronization map through dynamical consistency. The resulting sampled-data controller achieves small residual tracking errors without access to the governing equations. Relative to a reference map within the data-driven framework, the learned map reduces median control effort approximately eightfold while improving tracking accuracy. These results connect synchronization-map selection with conditional convergence guarantees and reduced control requirements.

Keywords: Increased-order generalized synchronization, Memristive neurons, Adaptive control, Lyapunov stability, Next generation reservoir computing, Data-driven control

1 Introduction

Synchronization is a fundamental phenomenon in nonlinear dynamics whereby interacting systems develop coordinated behavior. It establishes persistent relationships between phases, frequencies, or state trajectories, even when individual dynamics remain irregular. The central questions concern these relationships' existence, stability, and the coupling mechanisms that suppress deviations. These questions are particularly relevant when systems differ in parameters, timescales, or dimensions. Neural coordination has functional and pathological consequences: organized activity supports normal brain function [1], whereas excessive synchronization is associated with epileptic seizures [2]. Understanding synchronization therefore requires identifying its dynamical conditions and how coupling or control modifies them.

Chaotic synchronization shows that unstable trajectories can maintain a stable relationship. Pecora and Carroll demonstrated this in a drive–response configuration, where an autonomous chaotic system unidirectionally forces a response [3]. In complete synchronization, state trajectories asymptotically coincide, requiring compatible state spaces of equal dimension

[4]. Generalized synchronization instead describes a functional dependence of the response state on the drive state [5, 6]. Synchronization then corresponds to decaying deviations from a relation in the joint phase space. This viewpoint separates the complexity of synchronized motion from the relation's stability, providing a framework for nonidentical systems.

Unequal phase-space dimensions introduce a structural issue. Reduced-order synchronization concerns a response with fewer variables than the drive [7, 8], whereas increased-order generalized synchronization (IOGS) concerns a response with additional degrees of freedom [9–11]. IOGS must account for response variables without drive counterparts. Here, the relationship is designed: a target map is selected, and coupling drives the response toward its graph. The map determines the target motion and its mismatch with the intrinsic response dynamics. Its selection therefore affects the error equations, convergence conditions, and required forcing.

Memristive neuron models combine dimensional mismatch with memory, multiple timescales, and parameter uncertainty. The Hindmarsh–Rose (HR) model describes spiking and bursting by coupling membrane potential, fast recovery, and slow adaptation [12]. Memristive extensions add an internal state mediating activity-dependent feedback and modifying neuronal dynamics and synchronization [13, 14]. Additional adaptation processes increase the dimension and introduce dynamical pathways [8]. We consider a four-dimensional memristive HR drive and a five-dimensional response with an additional slow adaptation variable. Both include a switchable memristive element. This construction allows us to study coordination across unequal dimensions while retaining the memristive nonlinearity in the stability analysis.

Previous studies established increased-order synchronization using prescribed linear maps and active control with known parameters [9, 10]. Adaptive extensions address uncertain parameters, controlling additional response coordinates to reproduce a drive variable [15] or follow a prescribed function of the drive state [11]. For identical memristive HR neurons, Lyapunov analysis established local asymptotic stability of complete synchronization under dissipative memristive switching and practical stability with an explicit ultimate bound otherwise [16]. Reduced-order adaptive synchronization has also been studied for memristive HR neurons with parameter mismatch [8]. These results motivate studying increased-order synchronization with a nonlinear target map while retaining switching explicitly in the error dynamics. The problem balances feedback-induced dissipation against retained memristive dynamics while compensating parameter mismatch through adaptation.

A complementary difficulty arises when governing equations are unavailable or poorly known. Reconstructing neuronal dynamics from recordings is challenging [17], and data-driven methods enable prediction and control from observed trajectories [18]. Learned models serve as dynamical replicas and observers in synchronization research. A reservoir computer trained on a chaotic system can synchronize with it through an observed signal [19]. Reservoir observers infer unmeasured variables [20], enabling physical-response synchronization with reduced coupling strength [21]. Reservoir observers of memristive HR neurons with different dimensions have also achieved reduced-order synchronization [8]. These approaches demonstrate the usefulness of learned dynamics and raise a further question: how can they inform the target synchronization relationship?

Next generation reservoir computing (NG-RC) connects learned prediction with feedback control. NG-RC models compensate nonlinear dynamics and impose prescribed tracking-error decay in chaotic maps [22], with related schemes implemented on embedded hardware for a physical chaotic circuit [23]. Learning the synchronization map adds a geometric requirement: approximate compatibility with both systems' evolution. A related principle identifies conjugate mappings between Poincaré maps by enforcing consistency between coordinate transformation and dynamical evolution [24]. Here, we seek an approximately invariant graph under learned uncoupled dynamics. Advancing the drive and then mapping should approximately agree with mapping first and advancing the response. This criterion provides a self-supervised objective from uncoupled trajectories and measures the dynamical mismatch requiring control compensation. Exact conjugacy is not required.

We develop analytical and data-driven approaches centered on synchronization-map selection. The analytical approach prescribes a nonlinear map targeting all five response components while preserving the memristive coordinate. Feedback controllers and adaptive parameter-update laws retain switching explicitly in the error dynamics. Under the stated boundedness and existence assumptions, case-wise Lyapunov analysis proves asymptotic IOGS and bounded parameter-estimation errors when the memristive contribution

is uniformly strictly dissipative. Without this condition, a switching-independent estimate gives an explicit error radius outside which the adaptive Lyapunov function decreases, without asserting ultimate boundedness. Numerical simulations additionally exhibit synchronization-error decay along a trajectory that violates the strict dissipativity hypothesis, distinguishing the observed behavior from the suffcient conditions established analytically.

The data-driven approach trains memoryless NG-RC predictors on uncoupled full-state recordings with fixed response parameters. An affine synchronization map is learned through dynamical consistency, with variance and covariance penalties discouraging collapsed targets. The predictors and map define sampled-data coupling with additive actuation of every response component; governing equations generate and assess the experiments but are unavailable to the learning and control algorithms. The response tracks the learned target with small residual error. Within this framework, the learned map reduces median control effort approximately eightfold relative to the reference correspondence while improving tracking accuracy. These results illustrate complementary roles of map selection: retaining tractable error dynamics for conditional convergence guarantees and promoting dynamical compatibility to reduce forcing. The constructions use different maps and assumptions; the data-driven results provide neither a stability proof nor a direct performance comparison with the analytical controller.

The paper is organized as follows. Section 2 presents the neuronal models and uncontrolled dynamics. Section 3 develops the nonlinear synchronization map, controllers, and adaptive laws, and Section 4 establishes the analytical estimates. Section 5 relates numerical behavior to the theoretical conditions. Section 6 presents the learned predictors, synchronization map, and sampled-data control. Finally, Section 7 summarizes the findings and open directions.

2 Mathematical Models

To investigate increased-order generalized synchronization, we consider two extensions of the Hindmarsh–Rose (HR) model, a paradigmatic neuron model of established biological relevance: a four-dimensional memristive HR drive system and a controlled five-dimensional memristive HR response system with parameter mismatch. The underlying classical three-dimensional HR model [12] describes the interaction between the membrane potential, a fast recovery variable, and a slow adaptation current. Both the drive and response incorporate a switchable memristive autapse, while the response additionally includes an adaptation variable associated with slower ionic processes. This construction allows us to examine increased-order synchronization in the presence of both unequal phase-space dimensions and uncertain response parameters.

2.1 Drive and response neuronal systems

Let $\mathbf{X}_d = (x, y, z, u)^\top \in \mathbb{R}^4$ denote the drive state, where x is the membrane potential, y is the fast recovery variable, z represents the slow adaptation current, and u is the internal state of the switchable memristor [13]. The drive dynamics are given by

$$\dot{\mathbf{X}}_d = F_d(\mathbf{X}_d) = (F_1, F_2, F_3, F_4)^\top,$$

$$\begin{cases} F_1 := y - ax^3 + bx^2 + k(h + fu^2)x - z + I, \\ F_2 := c - px^2 - y, \\ F_3 := r[s(x - x_0) - z], \\ F_4 := -\xi u + mG(u) + x, \end{cases} \tag{1}$$

where

$$G(u) := |u + 1| - |u - 1| = \begin{cases} -2, & u < -1, \\ 2u, & -1 \le u \le 1, \\ 2, & u > 1. \end{cases} \tag{2}$$

The term $k(h + fu^2)x$ describes the memristive autaptic feedback [13]. Its strength is controlled by k, while h and f determine the state-independent and state-dependent contributions to the feedback coefficient, respectively. The memristor state is driven by the membrane potential and evolves under linear relaxation, $-\xi u$, and the continuous piecewise-linear switching term $mG(u)$. Thus, the membrane potential affects the internal memristor state, which in turn modulates the voltage dynamics, introducing an activity-dependent feedback mechanism. The parameter m controls the strength of the switching contribution.

The remaining terms retain their usual HR interpretation [12]. The coefficients a and b determine the cubic and quadratic voltage nonlinearities, c and p govern the fast recovery dynamics, and I is the applied current. The adaptation variable z relaxes towards $s(x - x_0)$ at

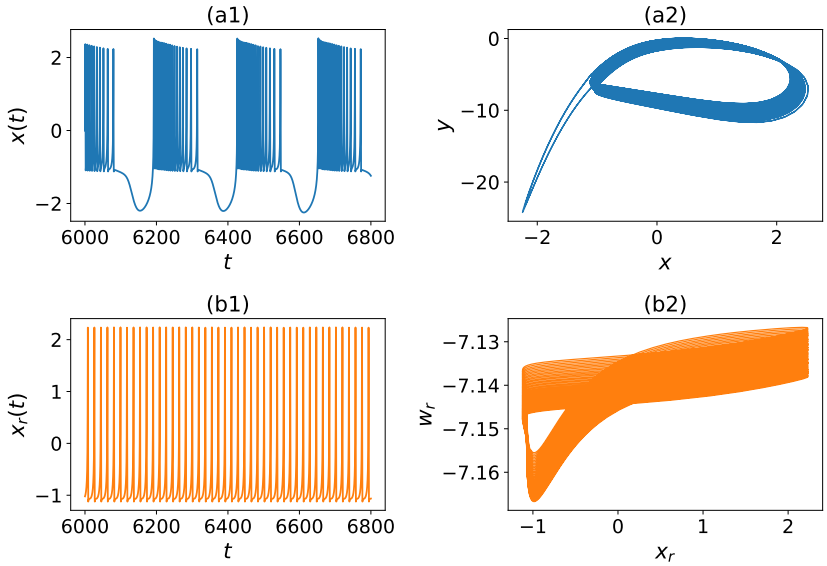

Figure 1 Uncontrolled dynamics at $I = 5.1$. (a1) Drive membrane potential $x(t)$ and (a2) trajectory projection onto the (x, y) plane. (b1) Response membrane potential $x_r(t)$ and (b2) trajectory projection onto the (x_r, w_r) plane. Voltage traces are shown for $t \in [6000, 6800]$. All other parameter values are as specified in the main text.

a rate determined by r and feeds back into the voltage equation through $-z$.

The response state is $\mathbf{X}_r = (x_r, y_r, z_r, u_r, w_r)^\top \in \mathbb{R}^5$. In addition to the four variables corresponding to those of the drive, the response contains an additional slow adaptation variable w_r, which phenomenologically represents the influence of slower ionic processes [8, 14]. Its controlled dynamics are

$$\begin{cases} \dot{x}_r = y_r - a x_r^3 + b x_r^2 + \bar{k}(h + f u_r^2) x_r \\ \qquad - z_r + I + v_1, \\ \dot{y}_r = c - p x_r^2 - y_r - \bar{\sigma} w_r + v_2, \\ \dot{z}_r = r[\bar{s}(x_r - x_0) - z_r] + v_3, \\ \dot{u}_r = -\bar{\xi} u_r + m G(u_r) + x_r + v_4, \\ \dot{w}_r = \bar{\eta}[\gamma(y_r - y_0) - \rho w_r] + v_5. \end{cases} \tag{3}$$

Here, $\mathbf{v} = (v_1, \ldots, v_5)^\top$ is the control vector to be designed in the subsequent synchronization analysis. The additional variable w_r phenomenologically represents calcium exchange between intracellular stores and the cytoplasm [25, 26]. It is driven by the deviation of the recovery variable y_r from the reference level y_0 and feeds back into the recovery equation through the term $-\bar{\sigma} w_r$. The parameters γ and ρ weight the recovery-dependent forcing and linear relaxation terms, respectively, while $\bar{\eta}$ scales the intrinsic dynamics of w_r. For $\bar{\eta}(t) > 0$ and $\rho > 0$, the linear decay term $-\bar{\eta}(t)\rho w_r$ defines an instantaneous relaxation rate $\bar{\eta}(t)\rho$, with corresponding timescale $[\bar{\eta}(t)\rho]^{-1}$. Consequently, the response extends the drive through an additional dynamical feedback pathway.

2.2 Parameter mismatch and nominal values

The time-dependent quantities $\bar{k}$, $\bar{\sigma}$, $\bar{s}$, $\bar{\xi}$, and $\bar{\eta}$ are adjustable response coefficients updated by the adaptive laws. They serve as estimates of the fixed nominal target parameters k, σ, s, ξ, and η, respectively. The parameters k, s, and ξ occur in the drive and have corresponding adjustable coefficients in the response. The parameters σ and η characterize the additional response pathway and have no counterparts in the four-dimensional drive.

Using the convention of estimate minus target, we define

$$\begin{aligned} &\hat{k} = \bar{k} - k, \quad \hat{\sigma} = \bar{\sigma} - \sigma, \quad \hat{s} = \bar{s} - s, \\ &\hat{\xi} = \bar{\xi} - \xi, \quad \hat{\eta} = \bar{\eta} - \eta. \end{aligned} \tag{4}$$

The nominal target values specify the numerical model and provide reference values for evaluating the parameter-estimation errors; they are not supplied to the adaptive controller. Unless stated otherwise, the

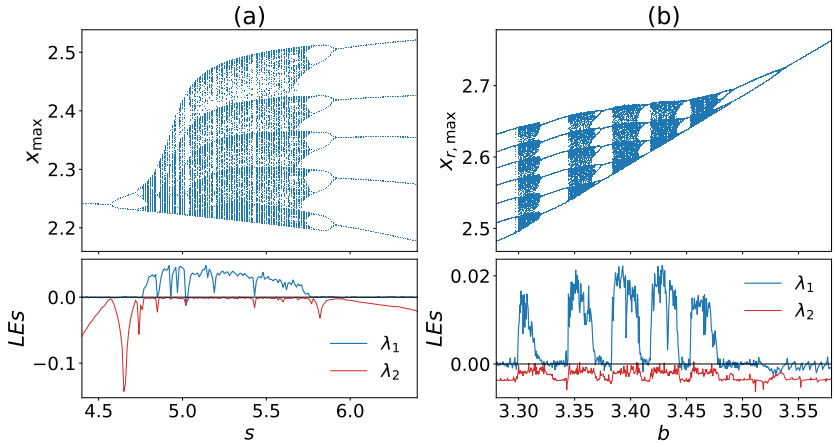

Figure 2 Bifurcation diagrams (top) and the corresponding two largest Lyapunov exponents $\lambda_1 \geq \lambda_2$ (bottom) for the uncontrolled drive and response systems, respectively. (a) Post-transient local maxima of $x(t)$ versus $s \in [4.40, 6.40]$, with $I = 5.0$ and $r = 0.02$. (b) Post-transient local maxima of $x_r(t)$ versus $b \in [3.28, 3.58]$. All other parameter values are as specified in the main text.

known parameters are fixed at $a = 1.0$, $b = 3.0$, $c = 1.0$, $p = 5.0$, $f = 0.2$, $h = 0.3$, $m = 0.5$, $r = 0.006$, $x_0 = -1.56$, $I = 3.1$, $y_0 = -1.619$, $\gamma = 3.0$, and $\rho = 0.9573$. The parameters y_0, γ, and ρ enter only the response system; the other known parameters are shared by both systems. The nominal target values are $k = 0.87$, $\sigma = 0.0278$, $s = 5.2$, $\xi = 1.0$, and $\eta = 0.0009$. The drive evolves with fixed values of k, s, and ξ, whereas the five adjustable response coefficients evolve according to the adaptive laws.

2.3 Models dynamics

To characterize the uncontrolled dynamics, we integrate Eqs. (1) and (3) independently with $\mathbf{v} = \mathbf{0}$ and $(\bar{k}, \bar{\sigma}, \bar{s}, \bar{\xi}, \bar{\eta}) = (k, \sigma, s, \xi, \eta)$, using the initial conditions

$$\mathbf{X}_d(0) = (0.1, 0.1, 0.1, 0.1)^\top,$$
$$\mathbf{X}_r(0) = (0.5, 0.5, 0.5, 0.5, 0)^\top.$$

Integration uses the adaptive Dormand–Prince Runge–Kutta method of order 5(4) [27], implemented as `RK45` in `SciPy` [28], with relative and absolute tolerances 10^{-6} and 10^{-8}, respectively.

Figure 1 illustrates some dynamical behaviors. After discarding the initial 6000 time units, the voltage traces over $t \in [6000, 6800]$ exhibit bursting in the drive and sustained spiking in the response. The corresponding trajectory projections illustrate the geometry of the dynamics.

To examine some parameter-dependent transitions, we construct numerical bifurcation diagrams from post-transient local maxima of $x(t)$ and $x_r(t)$ and estimate the two largest Lyapunov exponents, $\lambda_1 \geq \lambda_2$, from the associated variational equations using the Benettin algorithm. Figure 2 shows the dependence of the drive dynamics on s and the response dynamics on b. Intervals with $\lambda_1 > 0$ provide numerical evidence of chaos and are interspersed with windows consistent with periodic dynamics.

3 The IOGS problem: an analytical approach

We study an IOGS problem between the four-dimensional memristive HR drive system and the five-dimensional response system with parameter uncertainty. We first define a nonlinear map from the drive state space to the response state space, specifying a synchronization manifold and its associated error variables. This construction assigns a target to each response variable, including the additional adaptation variable w_r, which has no counterpart in the drive. We then formulate feedback controllers and adaptive parameter-update laws and derive the closed-loop error dynamics, retaining the memristive switching contribution explicitly. A case-wise analysis of this contribution identifies the switching configurations that ensure strict dissipation in the memristive error channel. These estimates form the basis for establishing our two main theoretical results: asymptotic IOGS under a uniform dissipativity condition on the memristive contribution, and a practical Lyapunov-type estimate without this condition. The latter provides an explicit error threshold above which the adaptive Lyapunov function is

strictly decreasing, but does not by itself establish ultimate boundedness of the synchronization error.

3.1 Nonlinear increased-order synchronization manifold

We define IOGS through a nonlinear map $\varphi : \mathbb{R}^4 \to \mathbb{R}^5$, which in the present work we choose as

$$\varphi(x, y, z, u) = (\varphi_1, \varphi_2, \varphi_3, \varphi_4, \varphi_5)^\top,$$
$$\begin{cases} \varphi_1 := x + \alpha_1 \sin x, \\ \varphi_2 := y + \alpha_2 x^2 + \alpha_3 u^2, \\ \varphi_3 := z + \alpha_4 xy, \\ \varphi_4 := u, \\ \varphi_5 := \beta_0 + \beta_1 x + \beta_2 y + \beta_3 z \\ \qquad + \beta_4 xu + \beta_5 \cos u. \end{cases} \tag{5}$$

Here $\alpha_1, \alpha_2, \alpha_3, \alpha_4, \beta_0, \beta_1, \beta_2, \beta_3, \beta_4, \beta_5 \in \mathbb{R}$. At least one nonlinear coefficient is assumed to be nonzero: $(\alpha_1, \alpha_2, \alpha_3, \alpha_4, \beta_4, \beta_5) \neq 0$.

The fourth component is chosen as $\varphi_4(x, y, z, u) = u$. This choice is crucial because it preserves the natural memristive error $e_4 = u_r - u$. Thus the switchable memristor contribution remains explicit in the error dynamics and is not hidden by the controller.

The IOGS error is defined by

$$\mathbf{e} = \mathbf{X}_r - \varphi(\mathbf{X}_d), \tag{6}$$

that is,

$$\begin{cases} e_1 = x_r - \Big(x + \alpha_1 \sin x\Big), \\ e_2 = y_r - \Big(y + \alpha_2 x^2 + \alpha_3 u^2\Big), \\ e_3 = z_r - \Big(z + \alpha_4 xy\Big), \\ e_4 = u_r - u, \\ e_5 = w_r - \Big(\beta_0 + \beta_1 x + \beta_2 y + \beta_3 z \\ \qquad + \beta_4 xu + \beta_5 \cos u\Big). \end{cases} \tag{7}$$

The associated IOGS manifold is

$$\mathcal{M}_{\mathrm{IOGS}} = \Big\{(\mathbf{X}_d, \mathbf{X}_r) \in \mathbb{R}^4 \times \mathbb{R}^5 : \mathbf{X}_r = \varphi(\mathbf{X}_d)\Big\}. \tag{8}$$

Definition 3.1 *The response system Eq. (3) is said to achieve increased-order generalized synchronization with the drive system Eq. (1) if*

$$\lim_{t\to\infty} \big\|\mathbf{X}_r(t) - \varphi(\mathbf{X}_d(t))\big\| = 0. \tag{9}$$

Definition 3.2 *The response system Eq. (3) is said to achieve practical increased-order generalized synchronization with the drive system Eq. (1) if there exists $\delta > 0$ such that*

$$\limsup_{t\to\infty} \big\|\mathbf{X}_r(t) - \varphi(\mathbf{X}_d(t))\big\| \leq \delta. \tag{10}$$

3.2 Controller design and adaptive laws

Since $e_i = X_{r,i} - \varphi_i(\mathbf{X}_d)$, we have

$$\dot{e}_i = \dot{X}_{r,i} - \dot{\varphi}_i(\mathbf{X}_d), \qquad i = 1, \ldots, 5. \tag{11}$$

The derivatives of the components of the nonlinear synchronization map are

$$\begin{cases} \dot{\varphi}_1 = (1 + \alpha_1 \cos x) F_1, \\ \dot{\varphi}_2 = F_2 + 2\alpha_2 x F_1 + 2\alpha_3 u F_4, \\ \dot{\varphi}_3 = F_3 + \alpha_4 y F_1 + \alpha_4 x F_2, \\ \dot{\varphi}_4 = F_4, \\ \dot{\varphi}_5 = (\beta_1 + \beta_4 u) F_1 + \beta_2 F_2 + \beta_3 F_3 \\ \qquad + (\beta_4 x - \beta_5 \sin u) F_4. \end{cases} \tag{12}$$

We introduce the response regressors

$$\begin{cases} \Phi_1 = (h + f u_r^2) x_r, \\ \Phi_2 = w_r, \\ \Phi_3 = r(x_r - x_0), \\ \Phi_4 = u_r, \\ \Phi_5 = \gamma(y_r - y_0) - \rho w_r. \end{cases} \tag{13}$$

Let $\lambda_1, \lambda_2, \lambda_3, \lambda_5 > 0$ and choose control inputs as

$$\begin{cases} v_1 = \dot{\varphi}_1 - \Big[y_r - a x_r^3 + b x_r^2 + k\Phi_1 - z_r + I\Big] \\ \qquad - \lambda_1 e_1, \\ v_2 = \dot{\varphi}_2 - \Big[c - p x_r^2 - y_r - \sigma\Phi_2\Big] - \lambda_2 e_2, \\ v_3 = \dot{\varphi}_3 - r\Big[s(x_r - x_0) - z_r\Big] - \lambda_3 e_3, \\ v_4 = x - x_r, \\ v_5 = \dot{\varphi}_5 - \eta\Phi_5 - \lambda_5 e_5. \end{cases} \tag{14}$$

The fourth controller $v_4 = x - x_r$ cancels only the direct mismatch induced by the membrane-potential term in the u-equation. It does not cancel the memristive switching difference $G(u_r) - G(u)$.

The adaptive update laws are selected as

$$\begin{cases} \dot{\hat{k}} = -\Phi_1 e_1, \\ \dot{\hat{\sigma}} = \Phi_2 e_2, \\ \dot{\hat{s}} = -\Phi_3 e_3, \\ \dot{\hat{\xi}} = \Phi_4 e_4, \\ \dot{\hat{\eta}} = -\Phi_5 e_5. \end{cases} \tag{15}$$

Since the target parameters are constant, the parameter-error dynamics satisfy

$$\begin{cases} \dot{\tilde{k}} = \dot{\hat{k}}, \\ \dot{\tilde{\sigma}} = \dot{\hat{\sigma}}, \\ \dot{\tilde{s}} = \dot{\hat{s}}, \\ \dot{\tilde{\xi}} = \dot{\hat{\xi}}, \\ \dot{\tilde{\eta}} = \dot{\hat{\eta}}. \end{cases} \tag{16}$$

Substituting Eq. (14) into the error equations in Eq. (11) gives the closed-loop adaptive error system

$$\begin{cases} \dot{e}_1 = -\lambda_1 e_1 + \hat{k}\Phi_1, \\ \dot{e}_2 = -\lambda_2 e_2 - \hat{\sigma}\Phi_2, \\ \dot{e}_3 = -\lambda_3 e_3 + \hat{s}\Phi_3, \\ \dot{e}_4 = -e_4 + m\Big[G(u_r) - G(u)\Big] - \hat{\xi}\Phi_4, \\ \dot{e}_5 = -\lambda_5 e_5 + \hat{\eta}\Phi_5. \end{cases} \tag{17}$$

3.3 Case-wise analysis of the memristive contribution

The memristive contribution to the Lyapunov derivative is

$$\Psi(e_4; u, u_r, m) := \Big[-e_4 + m\Big(G(u_r) - G(u)\Big)\Big]\, e_4, \quad e_4 = u_r - u. \tag{18}$$

Since $G(u)$ is given piecewise by Eq. (2), Ψ admits the following case-wise representation:

$$\Psi(e_4; u, u_r, m) = \begin{cases} -e_4^2, & \mathcal{C}_1 : \ u \geq 1, \ u_r \geq 1, \\ (2m-1)e_4^2 + 2m(u-1)e_4, & \mathcal{C}_2 : \ u \geq 1, \ -1 < u_r < 1, \\ -e_4^2 - 4me_4, & \mathcal{C}_3 : \ u \geq 1, \ u_r \leq -1, \\ -e_4^2 + 2m(1-u)e_4, & \mathcal{C}_4 : \ -1 < u < 1, \ u_r \geq 1, \\ (2m-1)e_4^2, & \mathcal{C}_5 : \ -1 < u < 1, \ -1 < u_r < 1, \\ -e_4^2 - 2m(1+u)e_4, & \mathcal{C}_6 : \ -1 < u < 1, \ u_r \leq -1, \\ -e_4^2 + 4me_4, & \mathcal{C}_7 : \ u \leq -1, \ u_r \geq 1, \\ (2m-1)e_4^2 + 2m(u+1)e_4, & \mathcal{C}_8 : \ u \leq -1, \ -1 < u_r < 1, \\ -e_4^2, & \mathcal{C}_9 : \ u \leq -1, \ u_r \leq -1. \end{cases} \tag{19}$$

For $e_4 \neq 0$, define the normalized memristive coefficient

$$\Theta(u, u_r, m) = \frac{\Psi(e_4; u, u_r, m)}{e_4^2}. \tag{20}$$

The trajectory is said to remain in a strictly dissipative memristive switching regime if there exists $\mu > 0$ such that

$$\Theta(u(t), u_r(t), m) \leq -\mu, \qquad t \geq 0. \tag{21}$$

Equivalently, $\Psi(e_4(t); u(t), u_r(t), m) \leq -\mu e_4^2(t)$ for all $t \geq 0$.

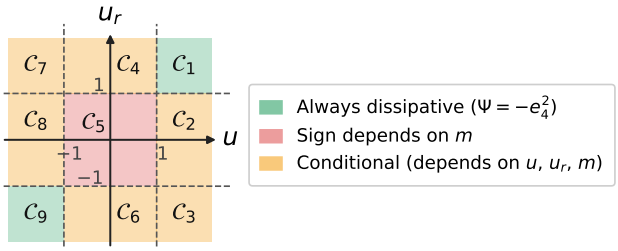

Figure 3 Partition of the (u, u_r) plane into the nine switching cases $\mathcal{C}_1, \ldots, \mathcal{C}_9$ of Ψ defined in Eq. (19). Green regions ($\mathcal{C}_1$, $\mathcal{C}_9$) are always dissipative, with $\Psi = -e_4^2$. The red region ($\mathcal{C}_5$) has a sign that depends on m. Amber regions are conditional, with dissipativity depending on the trajectory $(u(t), u_r(t))$ and m.

More explicitly, the dissipative switching set associated with a given $\mu > 0$ is

$$\mathcal{D}_\mu = \left\{ (u, u_r) : \Psi(e_4; u, u_r, m) \le -\mu e_4^2 \right\}. \tag{22}$$

Using Eq. (19), this set is the union of the following case-wise regions:

$$\begin{aligned}
\mathcal{D}_\mu = \mathcal{C}_1 \cup \mathcal{C}_9 \\
\cup \left\{ \mathcal{C}_2 : (2m-1)e_4^2 + 2m(u-1)e_4 \le -\mu e_4^2 \right\} \\
\cup \left\{ \mathcal{C}_3 : -e_4^2 - 4me_4 \le -\mu e_4^2 \right\} \\
\cup \left\{ \mathcal{C}_4 : -e_4^2 + 2m(1-u)e_4 \le -\mu e_4^2 \right\} \\
\cup \left\{ \mathcal{C}_5 : (2m-1)e_4^2 \le -\mu e_4^2 \right\} \\
\cup \left\{ \mathcal{C}_6 : -e_4^2 - 2m(1+u)e_4 \le -\mu e_4^2 \right\} \\
\cup \left\{ \mathcal{C}_7 : -e_4^2 + 4me_4 \le -\mu e_4^2 \right\} \\
\cup \left\{ \mathcal{C}_8 : (2m-1)e_4^2 + 2m(u+1)e_4 \le -\mu e_4^2 \right\}.
\end{aligned} \tag{23}$$

Thus, the purely outer cases $\mathcal{C}_1$ and $\mathcal{C}_9$ are always dissipative with $\mu \le 1$. The remaining cases may be dissipative or non-dissipative depending on m and on the instantaneous position of the trajectory within the corresponding switching region. Figure 3 illustrates the nine switching cases in the (u, u_r) plane, color-coded by their dissipativity character.

The complementary set $\mathcal{N}_\mu = \mathbb{R}^2 \setminus \mathcal{D}_\mu$ is referred to as the non-dissipative memristive switching set. In this set, the strict estimate $\Psi(e_4; u, u_r, m) \le -\mu e_4^2$ is not guaranteed. The following section establishes our main theoretical results, first under the uniform dissipativity condition and then without this restriction.

4 Main theoretical results on IOGS

We now establish the two main theoretical results of this paper using the closed-loop error dynamics and the estimates for the memristive contribution derived above.

4.1 Adaptive asymptotic IOGS under dissipative memristive switching

When the trajectory $(u(t), u_r(t))$ remains in $\mathcal{D}_\mu$ for some fixed $\mu > 0$, the adaptive laws and the uniform dissipativity estimate yield a Lyapunov inequality that ensures asymptotic convergence of the synchronization error. The following theorem states the required assumptions and establishes boundedness of the parameter-estimation errors.

Theorem 4.1 *Consider the drive system Eq. (1), the controlled response system Eq. (3), and the nonlinear synchronization map Eq. (5). Let the controllers be given by Eq. (14), and let the adaptive laws be given by Eq. (15). Assume that the drive trajectory is bounded and that the closed-loop solution exists for all $t \ge 0$. Assume further that the memristive switching trajectory remains in the dissipative set $\mathcal{D}_\mu$ for some constant $\mu > 0$, that is, $(u(t), u_r(t)) \in \mathcal{D}_\mu$ for all $t \ge 0$, equivalently*

$$\Psi(e_4(t); u(t), u_r(t), m) \le -\mu e_4^2(t), \qquad t \ge 0. \tag{24}$$

Then the increase-order synchronization error satisfies

$$\lim_{t\to\infty} \|\mathbf{e}(t)\| = 0. \tag{25}$$

Consequently, the response system achieves increased-order generalized synchronization with the drive system:

$$\lim_{t\to\infty} \left\| \mathbf{X}_r(t) - \varphi(\mathbf{X}_d(t)) \right\| = 0. \tag{26}$$

Moreover, the parameter-estimation errors remain bounded.

Proof Consider the adaptive Lyapunov function

$$\begin{aligned}
V = \frac{1}{2}\Big(e_1^2 + e_2^2 + e_3^2 + e_4^2 + e_5^2 \\
+ \hat{k}^2 + \hat{\sigma}^2 + \hat{s}^2 + \hat{\xi}^2 + \hat{\eta}^2 \Big) \ge 0.
\end{aligned} \tag{27}$$

Along trajectories of Eq. (17),

$$\begin{aligned}
\dot{V} = e_1\dot{e}_1 + e_2\dot{e}_2 + e_3\dot{e}_3 + e_4\dot{e}_4 + e_5\dot{e}_5 \\
+ \hat{k}\dot{\hat{k}} + \hat{\sigma}\dot{\hat{\sigma}} + \hat{s}\dot{\hat{s}} + \hat{\xi}\dot{\hat{\xi}} + \hat{\eta}\dot{\hat{\eta}}.
\end{aligned} \tag{28}$$

Substituting Eq. (17) gives

$$\begin{aligned}
\dot{V} = & -\lambda_1 e_1^2 + \Phi_1 \hat{k} e_1 - \lambda_2 e_2^2 - \Phi_2 \hat{\sigma} e_2 \\
& - \lambda_3 e_3^2 + \Phi_3 \hat{s} e_3 - e_4^2 \\
& + \left[m\big(G(u_r) - G(u)\big) - \Phi_4 \hat{\xi} \right] e_4 \\
& - \lambda_5 e_5^2 + \Phi_5 \hat{\eta} e_5 \\
& + \hat{k}\dot{\hat{k}} + \hat{\sigma}\dot{\hat{\sigma}} + \hat{s}\dot{\hat{s}} + \hat{\xi}\dot{\hat{\xi}} + \hat{\eta}\dot{\hat{\eta}}.
\end{aligned} \tag{29}$$

Using the adaptive laws Eq. (15), all parameter-error cross terms cancel:

$$\begin{aligned}
&\Phi_1 \hat{k} e_1 + \hat{k}\dot{\hat{k}} = 0, \quad && -\Phi_2 \hat{\sigma} e_2 + \hat{\sigma}\dot{\hat{\sigma}} = 0, \\
&\Phi_3 \hat{s} e_3 + \hat{s}\dot{\hat{s}} = 0, \quad && -\Phi_4 \hat{\xi} e_4 + \hat{\xi}\dot{\hat{\xi}} = 0, \\
&\Phi_5 \hat{\eta} e_5 + \hat{\eta}\dot{\hat{\eta}} = 0.
\end{aligned} \tag{30}$$

Therefore,

$$\dot{V} = -\lambda_1 e_1^2 - \lambda_2 e_2^2 - \lambda_3 e_3^2 - \lambda_5 e_5^2 + \Psi(e_4; u, u_r, m). \tag{31}$$

Since $(u(t), u_r(t)) \in \mathcal{D}_\mu$, the case-wise definition Eq. (22) gives $\Psi(e_4; u, u_r, m) \le -\mu e_4^2$. Thus

$$\dot{V} \le -\lambda_1 e_1^2 - \lambda_2 e_2^2 - \lambda_3 e_3^2 - \mu e_4^2 - \lambda_5 e_5^2. \tag{32}$$

Let $\alpha = \min\{\lambda_1, \lambda_2, \lambda_3, \mu, \lambda_5\} > 0$. Then

$$\dot{V} \le -\alpha \|\mathbf{e}\|^2. \tag{33}$$

Hence $V(t) \le V(0)$ for all $t \ge 0$. Therefore, the synchronization errors and the parameter-estimation errors are bounded. Since the drive trajectory is bounded (consistent with the existence of chaotic attractors in the HR neuron model, which is observed numerically) and $\mathbf{X}_r = \mathbf{e} + \varphi(\mathbf{X}_d)$, the response trajectory is bounded as well. Consequently, the regressors Φ_i, $i = 1, \ldots, 5$ in Eq. (13) are bounded. From Eq. (17), it follows that $\dot{\mathbf{e}} \in L^\infty$.

Lemma 4.1 (Barbalat's Lemma) *Let $g : [0, \infty) \to \mathbb{R}$ be uniformly continuous and suppose that $\int_0^t g(s)\, ds$ has a finite limit as $t \to \infty$. Then $\lim_{t\to\infty} g(t) = 0$.*

Integrating Eq. (33) from 0 to t, we obtain

$$V(t) - V(0) \le -\alpha \int_0^t \|\mathbf{e}(\tau)\|^2 \, d\tau.$$

Since $V(t) \ge 0$, this implies $\int_0^t \|\mathbf{e}(\tau)\|^2 \, d\tau \le \frac{V(0)}{\alpha}$, $t \ge 0$. Hence, $\|\mathbf{e}(\cdot)\|^2 \in L^1([0, \infty))$.

Let $g(t) = \|\mathbf{e}(t)\|^2$ so that

$$\dot{g} = \frac{d}{dt}\|\mathbf{e}(t)\|^2 = 2\mathbf{e}(t)^\top \dot{\mathbf{e}}(t).$$

Since $\mathbf{e} \in L^\infty$ and $\dot{\mathbf{e}} \in L^\infty$, the function g is Lipschitz and uniformly continuous on $[0, \infty)$. By Barbalat's lemma, $\lim_{t\to\infty} \|\mathbf{e}(t)\|^2 = 0$, and by the continuity of the square-root function, we have $\lim_{t\to\infty} \|\mathbf{e}(t)\| = 0$. Because $\mathbf{e}(t) = \mathbf{X}_r(t) - \varphi(\mathbf{X}_d(t))$, we conclude that

$$\lim_{t\to\infty} \|\mathbf{X}_r(t) - \varphi(\mathbf{X}_d(t))\| = 0.$$

This is precisely the condition in Definition 3.1. Hence the response system achieves increased-order generalized synchronization with the drive system. Boundedness of the parameter-estimation errors follows from the boundedness of $V(t)$. □

4.2 Adaptive practical Lyapunov-type estimate under non-dissipative memristive switching

When the trajectory $(u(t), u_r(t))$ lies outside $\mathcal{D}_\mu$, the prescribed uniform dissipativity condition is not satisfied. Nevertheless, the following theorem establishes a practical Lyapunov-type estimate valid irrespective of the active switching region and identifies an explicit error threshold above which the adaptive Lyapunov function is strictly decreasing.

Theorem 4.2 *Consider the same drive-response systems, synchronization map, controllers, and adaptive laws as in Theorem 4.1. Suppose that the closed-loop solution exists for all $t \ge 0$ and let $\varepsilon \in (0, 2)$. Define*

$$C = \frac{8m^2}{\varepsilon}, \qquad \alpha = \min\left\{\lambda_1, \lambda_2, \lambda_3, \lambda_5, 1 - \frac{\varepsilon}{2}\right\}. \tag{34}$$

If $\alpha > 0$, then the adaptive Lyapunov function Eq. (27) satisfies

$$\dot{V}(t) \le -\alpha \|\mathbf{e}(t)\|^2 + C. \tag{35}$$

Consequently, $\dot{V}(t) < 0$ whenever $\|\mathbf{e}(t)\| > \sqrt{C/\alpha}$, so that the adaptive Lyapunov function decreases whenever the synchronization error lies outside the ball of radius

$$\delta = \sqrt{\frac{C}{\alpha}} = \sqrt{\frac{8m^2}{\varepsilon\alpha}}. \tag{36}$$

Therefore, the closed-loop system satisfies a practical Lyapunov-type bound with respect to the increased-order synchronization error. Equivalently, the adaptive Lyapunov function is strictly decreasing outside the error neighborhood

$$\mathcal{B}_\delta(\mathcal{M}_{\mathrm{IOGS}}) = \left\{(\mathbf{X}_d, \mathbf{X}_r) : \left\|\mathbf{X}_r - \varphi(\mathbf{X}_d)\right\| \le \delta\right\}. \tag{37}$$

Proof Using the adaptive Lyapunov function Eq. (27) and repeating the cancellation argument from the proof of Theorem 4.1, we again arrive at Eq. (31), that is,

$$\dot{V} = -\lambda_1 e_1^2 - \lambda_2 e_2^2 - \lambda_3 e_3^2 - \lambda_5 e_5^2 + \Psi(e_4; u, u_r, m).$$

It remains to bound the memristive contribution $\Psi(e_4; u, u_r, m)$ under non-dissipative switching. By Eq. (18),

$$\Psi(e_4; u, u_r, m) = -e_4^2 + m\big[G(u_r) - G(u)\big]e_4.$$

Since $|G(u)| \le 2$ for all $u \in \mathbb{R}$, the triangle inequality gives $|G(u_r) - G(u)| \le |G(u_r)| + |G(u)| \le 4$, so that

$$m\big[G(u_r) - G(u)\big]e_4 \le |m|\,|G(u_r) - G(u)|\,|e_4| \le 4|m||e_4|.$$

By Young's inequality, for every $\varepsilon > 0$,

$$4|m||e_4| \le \frac{\varepsilon}{2} e_4^2 + \frac{8m^2}{\varepsilon}.$$

Therefore,

$$\Psi(e_4; u, u_r, m) \le -\left(1 - \frac{\varepsilon}{2}\right) e_4^2 + \frac{8m^2}{\varepsilon}.$$

Substituting this estimate into the expression for $\dot{V}$, we obtain

$$\dot{V} \le -\lambda_1 e_1^2 - \lambda_2 e_2^2 - \lambda_3 e_3^2 - \lambda_5 e_5^2 - \left(1 - \frac{\varepsilon}{2}\right) e_4^2 + \frac{8m^2}{\varepsilon}.$$

Using the definitions of C and α in Eq. (34), this becomes

$$\dot{V} \le -\alpha \|\mathbf{e}\|^2 + C,$$

which is precisely Eq. (35). Consequently, if $\|\mathbf{e}(t)\|^2 > C/\alpha$, then $\dot{V}(t) < 0$. Since $\mathbf{e}(t) = \mathbf{X}_r(t) - \varphi(\mathbf{X}_d(t))$, this ball corresponds to the error neighborhood Eq. (37) with radius $\delta = \sqrt{C/\alpha} = \sqrt{8m^2/(\varepsilon\alpha)}$. Thus the closed-loop system satisfies a practical Lyapunov-type bound with respect to the increased-order synchronization error, which proves the stated estimate. □

Remark 4.1 The estimate in Theorem 4.2 identifies the neighborhood appearing in Definition 3.2 as the natural practical synchronization neighborhood. However, without an additional ultimate-boundedness argument (which is beyond the scope of the current manuscript), it should be interpreted as a Lyapunov-type decrease condition rather than as a proof of the full lim sup-condition in Definition 3.2.

Remark 4.2 The asymptotic result requires that the trajectory remains in the dissipative switching set $\mathcal{D}_\mu$. This assumption is case-wise and explicit: at each time, the active switching case in Eq. (19) satisfies the corresponding inequality listed in Eq. (23). The complementary set $\mathcal{N}_\mu$ contains the switching configurations for which strict dissipation cannot be guaranteed. In these configurations, the memristive term may inject a non-dissipative residual into the Lyapunov derivative, and the appropriate conclusion is a practical Lyapunov-type estimate rather than exact asymptotic IOGS.

Remark 4.3 The adaptive laws Eq. (15) guarantee boundedness of the parameter-estimation errors and cancellation of the corresponding cross terms in the Lyapunov derivative. However, convergence of $\bar{k}, \bar{\sigma}, \bar{s}, \bar{\xi}, \bar{\eta}$ to their target values generally requires additional persistence-of-excitation conditions on the regressors Φ_i. Without such excitation assumptions, the synchronization errors may converge to zero while the parameter estimates converge only to constant values.

Remark 4.4 The fourth component of the synchronization map is chosen as $\varphi_4(x, y, z, u) = u$. Therefore, the memristive synchronization error is exactly $e_4 = u_r - u$. This choice prevents the switchable memristive nonlinearity from being removed by control. Instead, the term $m\big[G(u_r) - G(u)\big]$ is retained explicitly in the closed-loop error dynamics and treated by case-wise Lyapunov estimates. This yields two regimes: exact asymptotic increased-order generalized synchronization when the trajectory remains in the dissipative switching set $\mathcal{D}_\mu$, and a practical Lyapunov-type estimate with an explicit radius when strict dissipativity is not guaranteed.

Remark 4.5 The practical Lyapunov-type radius $\delta = \sqrt{8m^2/(\varepsilon\alpha)}$ depends on the memristive strength m, the Young parameter ε, and the effective dissipation rate $\alpha = \min\{\lambda_1, \lambda_2, \lambda_3, \lambda_5, 1 - \varepsilon/2\}$. Increasing the feedback gains λ_i increases the dissipative contribution of the controlled channels, while the factor $1 - \varepsilon/2$ measures the remaining dissipation in the memristive channel after the Young estimate has been applied.

5 Numerical corroboration of IOGS and discussion

To assess the adaptive IOGS scheme numerically, we integrate the full closed-loop drive–response–adaptation system. Its fourteen state variables comprise the drive state $X_d \in \mathbb{R}^4$, the response state $X_r \in \mathbb{R}^5$, and the five adaptive parameter estimates $\bar{k}$, $\bar{\sigma}$, $\bar{s}$, $\bar{\xi}$, and $\bar{\eta}$. Combining the drive and response systems in Eqs. (1) and (3) with the controllers in Eq. (14) and the adaptive laws in Eq. (15) yields

$$\begin{cases} \dot{x} = F_1, \quad \dot{y} = F_2, \quad \dot{z} = F_3, \quad \dot{u} = F_4, \\ \dot{x}_r = y_r - a x_r^3 + b x_r^2 + \bar{k}(h + f u_r^2) x_r \\ \qquad - z_r + I + v_1, \\ \dot{y}_r = c - p x_r^2 - y_r - \bar{\sigma} w_r + v_2, \\ \dot{z}_r = r\Big[\bar{s}(x_r - x_0) - z_r\Big] + v_3, \\ \dot{u}_r = -\bar{\xi} u_r + m G(u_r) + x_r + v_4, \\ \dot{w}_r = \bar{\eta}\Big[\gamma(y_r - y_0) - \rho w_r\Big] + v_5, \\ \dot{\bar{k}} = -\Phi_1 e_1, \quad \dot{\bar{\sigma}} = \Phi_2 e_2, \quad \dot{\bar{s}} = -\Phi_3 e_3, \\ \dot{\bar{\xi}} = \Phi_4 e_4, \quad \dot{\bar{\eta}} = -\Phi_5 e_5. \end{cases} \tag{38}$$

IOGS is assessed through the five components of $\mathbf{e}(t) = X_r(t) - \varphi(X_d(t))$ and their Euclidean norm

$$\|\mathbf{e}(t)\| = \left(\sum_{i=1}^{5} e_i^2(t) \right)^{1/2}. \tag{39}$$

Decay of these quantities toward zero over the simulated interval provides numerical evidence of asymptotic IOGS.

The numerical results are also interpreted in relation to the practical Lyapunov-type estimate of Theorem 4.2. In particular, we examine the sign of the memristive contribution and its implications for the evolution of the adaptive Lyapunov function.

The drive is initialized at $X_d(0) = (0.1, 0.1, 0.1, 0.1)^\top$, as in Section 2.3. For the synchronization map, we set $\alpha_1 = \alpha_2 = \alpha_3 = \alpha_4 = 0.1$ and $(\beta_0, \ldots, \beta_5) = (0, 1, 1, 0, 0.1, 0.1)$. The response initial condition is prescribed by $X_r(0) = \varphi(X_d(0)) + (1, 1, 1, 1, -1)^\top$, ensuring $\mathbf{e}(0) = (1, 1, 1, 1, -1)^\top$ and giving $X_r(0) \approx$

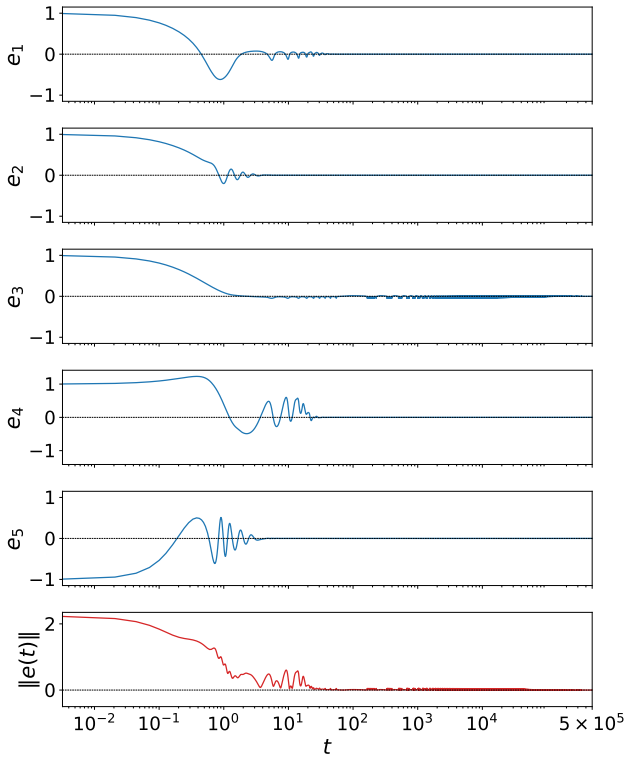

Figure 4 Time evolution of the synchronization errors $e_1(t), \ldots, e_5(t)$ and their Euclidean norm $\|e(t)\|$. Logarithmic time axes resolve the transient oscillations and the subsequent relaxation toward zero.

$(1.1100, 1.1020, 1.1010, 1.1000, -0.6995)^\top$. All five adaptive parameter estimates are initialized at zero, and the feedback gains are fixed at $\lambda_1 = \lambda_2 = \lambda_3 = \lambda_5 = 2$. We integrate Eq. (38) over $t \in [0, 5 \times 10^5]$ using the numerical method and tolerances specified in Section 2.3. The results are displayed on logarithmic time axes to resolve both the initial transient and the subsequent slow relaxation.

Figure 4 shows the synchronization errors and their Euclidean norm. Following transient overshoots and oscillations, all five components approach zero, with e_3 exhibiting a longer relaxation than the other components. The error norm decreases nonmonotonically, reaching approximately 6.19×10^{-7} at the final integration time. Its maximum observed value over the final 20% of the simulated interval is 1.22×10^{-5}. These results are consistent with asymptotic IOGS for the trajectory considered.

Figure 5 shows the parameter-estimation errors $\widehat{k}(t)$, $\widehat{\sigma}(t)$, $\widehat{s}(t)$, $\widehat{\xi}(t)$, and $\widehat{\eta}(t)$, defined previously as the differences between the adaptive estimates and their

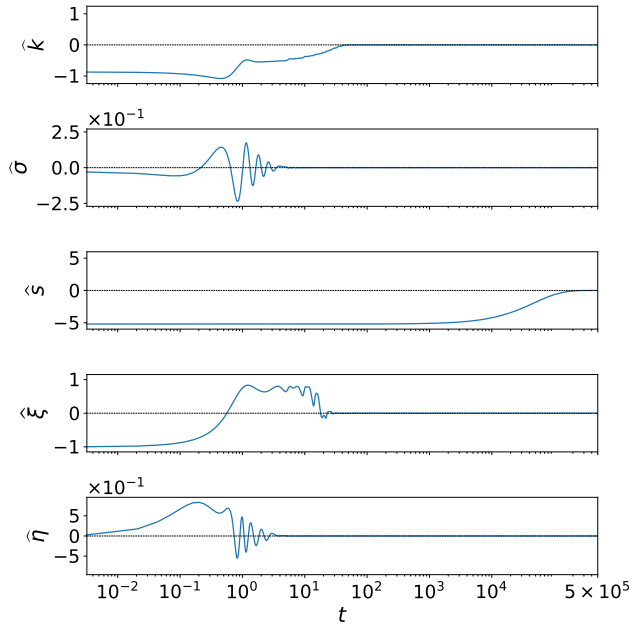

Figure 5 Time evolution of the parameter-estimation errors $\widehat{k}(t)$, $\widehat{\sigma}(t)$, $\widehat{s}(t)$, $\widehat{\xi}(t)$, and $\widehat{\eta}(t)$ relative to the nominal target values. Logarithmic time axes reveal the distinct relaxation times, with $\widehat{s}(t)$ approaching zero substantially more slowly than the other components.

nominal target values. All five errors approach zero over the simulated interval, although the relaxation of $\widehat{s}$ is substantially slower than that of the other components. At the final integration time, $\widehat{s} \approx -1.53 \times 10^{-4}$, while the absolute values of the remaining parameter-estimation errors are below 3×10^{-9}. These values indicate accurate recovery of the nominal parameters for the computed trajectory. Synchronization alone, however, does not imply parameter identification. A theoretical guarantee of convergence of the adaptive estimates to their targets requires additional analysis, typically involving excitation conditions on the regressors; such conditions, beyond the scope of the current study, are not established here.

We next examine the memristive contribution to the Lyapunov derivative along the computed trajectory. Figure 6 shows the previously defined quantities $\Psi(t)$ and $\Theta(t) = \Psi(t)/e_4^2(t)$. The normalized coefficient is evaluated only where $e_4(t)$ remains numerically resolved, since division by $e_4^2(t)$ becomes sensitive to numerical errors as $e_4(t)$ approaches zero. The uniform dissipativity assumption of Theorem 4.1 requires

a fixed $\mu > 0$ such that

$$\Psi(t) \le -\mu e_4^2(t) \qquad \text{for all } t \ge 0,$$

or, equivalently, $\Theta(t) \le -\mu$ whenever $e_4(t) \neq 0$.

For the chosen value $m = 0.5$, monotonicity and the 2-Lipschitz continuity of G imply

$$\Theta(t) = -1 + \frac{1}{2}\frac{G(u_r(t)) - G(u(t))}{u_r(t) - u(t)} \in [-1, 0], \quad e_4(t) \neq 0.$$

Thus, the memristive contribution is nonpositive throughout the trajectory. In particular, $\Theta = -1$ when both memristive states occupy the same outer branch ($\mathcal{C}_1$ or $\mathcal{C}_9$), whereas $\Theta = 0$ when both occupy the central branch ($\mathcal{C}_5$).

As shown in Figure 6, the trajectory repeatedly enters $\mathcal{C}_5$ while e_4 remains nonzero and numerically resolved. These visits preclude any fixed $\mu > 0$ satisfying the uniform dissipativity condition for all $t \ge 0$. Consequently, Theorem 4.1 does not directly establish asymptotic IOGS for this particular trajectory, despite the observed decay of the synchronization errors. Thus, the simulation provides numerical evidence of synchronization beyond the *sufficient* conditions of Theorem 4.1, rather than a numerical corroboration of that theorem under its stated hypotheses.

The switching-independent estimate of Theorem 4.2 remains applicable under its stated assumptions. It provides a Lyapunov decrease condition outside the prescribed error neighborhood, but does not by itself establish ultimate boundedness or asymptotic convergence. For the present parameter choice, the stronger sign property $\Psi \le 0$ implies $\dot{V} \le 0$ and hence boundedness of the synchronization and parameter-estimation errors. This nonincrease of V, however, does not by itself imply $e_4(t) \to 0$. The observed decay of the memristive error is therefore a numerical finding beyond the convergence conclusions established by the present Lyapunov analysis, and is compatible with the estimate of Theorem 4.2.

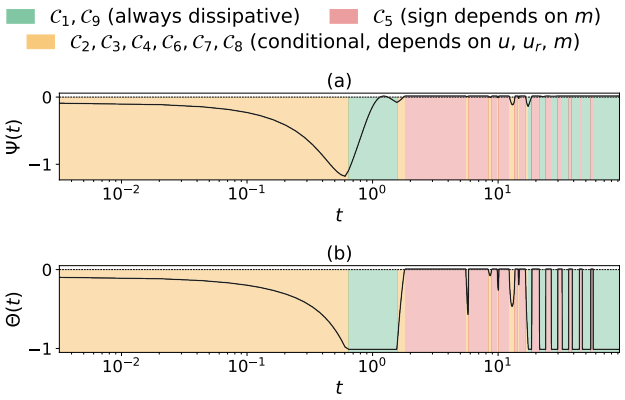

Figure 6 Memristive dissipation along the computed trajectory for $m = 0.5$: (a) Lyapunov contribution $\Psi(t)$ and (b) normalized coefficient $\Theta(t)$. The displayed interval is restricted to times for which $e_4(t)$ remains numerically resolved. Background shading identifies the active switching case, using the convention of Figure 3. Visits to the central region $\mathcal{C}_5$ yield $\Theta = 0$ for nonzero e_4, so the uniform strict dissipativity condition is not satisfied, although $\Psi \le 0$ throughout.

6 The IOGS problem: a data-driven approach

In this section, we tackle the IOGS problem through the lens of machine learning. For a complex system, accurate governing equations may be unavailable, with only measurements of its activity—such as membrane potentials and ionic currents in neural systems—accessible. Data-driven approaches therefore offer a means of designing control schemes directly from observed dynamics.

In this paper, we address IOGS under the assumption that the full states of both systems are sampled at interval Δt and that the control input enters the response additively, as in Eq. (3). From uncoupled state trajectories, Next Generation Reservoir Computing (NG-RC) [29] learns one-step predictors of the drive and response dynamics (Section 6.1). We then replace the prescribed analytical map φ in Eq. (5) with a parameterized map φ_θ, learned through a self-supervised objective that promotes consistency between the two predictors without requiring paired drive–response observations (Section 6.2). The learned predictors and map define a sampled-data coupling law (Section 6.3). The governing equations are used only to generate the recordings and simulate the controlled dynamics; they are not supplied to the learning or control algorithms. The complete procedure, comprising offline learning of the predictors and synchronization map followed by online sampled-data control, is summarized in Algorithm 1 in the Appendix A.

6.1 Next generation reservoir computing

Our goal is to learn approximations $\hat{F}_d$ and $\hat{F}_r$ of the drive vector field F_d in Eq. (1) and the uncontrolled response vector field F_r, defined by the right-hand side

of Eq. (3) with $\mathbf{v} = \mathbf{0}$, from sampled trajectories alone. Here, hats denote learned quantities rather than parameter errors as in Eq. (4). To this end, we use NG-RC [29], which replaces the randomly connected recurrent reservoir of an echo state network [30] with an explicit feature vector comprising state variables, optional time delays, and their monomials (Figure 7).

Training and assessment data are generated by simulating the two systems independently, with the response parameters fixed at the nominal values specified in Section 2.2, namely $(\bar{k}, \bar{\sigma}, \bar{s}, \bar{\xi}, \bar{\eta}) = (k, \sigma, s, \xi, \eta)$. Trajectories are sampled at interval $\Delta t = 0.02$. We write $\mathbf{X}(t) \in \mathbb{R}^n$ for either sampled state, with $n = 4$ for the drive and $n = 5$ for the response. Recordings from distinct initial conditions are partitioned into disjoint training, evaluation, and test sets, assigning each recording entirely to one set. The training set is used to fit the readout matrix $\mathbf{W}_{\text{out}}$, the evaluation set to select hyperparameters, and the held-out test set to assess generalization to unseen trajectories. States are standardized as $\tilde{\mathbf{X}}(t) = \mathbf{D}^{-1}(\mathbf{X}(t) - \bar{\mathbf{X}})$, where $\bar{\mathbf{X}}$ contains the componentwise training means and $\mathbf{D} = \operatorname{diag}(d_1, \ldots, d_n)$ contains the corresponding standard deviations, assumed positive. These training statistics are also used to standardize the evaluation and test data.

Unlike [29], and following [22], we use a memoryless formulation. For the deterministic systems considered here, the full state determines the subsequent evolution, so delay coordinates are not required. This also permits evaluating $\hat{F}_r$ at mapped drive states (Section 6.2) and controlled response states (Section 6.3), for which an uncontrolled response history is unavailable. The nonlinear features $\mathbf{O}_{\text{nonlin}}(t)$ comprise all distinct monomials of total degree 2 through q in the standardized state components, giving

$$\mathbf{O}(t) = \Big[1;\ \tilde{\mathbf{X}}(t);\ \mathbf{O}_{\text{nonlin}}(t)\Big]. \tag{40}$$

Following [29], we train the readout on consecutive state increments, scaled here to standardized finite-difference rates $\mathbf{Y}(t) = \Big(\tilde{\mathbf{X}}(t + \Delta t) - \tilde{\mathbf{X}}(t)\Big)/\Delta t$. Stacking features and targets column-wise over the training recordings yields the matrices $\mathbf{O}$ and $\mathbf{Y}$. Ridge regression then gives

$$\mathbf{W}_{\text{out}} = \mathbf{Y}\mathbf{O}^{\top}\Big(\mathbf{O}\mathbf{O}^{\top} + \nu\mathbf{I}\Big)^{-1}, \tag{41}$$

where $\nu > 0$ is the Tikhonov regularization parameter.

In the original coordinates, $\hat{F}(\mathbf{X}) := \mathbf{D}\mathbf{W}_{\text{out}}\mathbf{O}(\mathbf{X})$ approximates the finite-time increment rate $\Big(\Phi_{\Delta t}(\mathbf{X}) - \mathbf{X}\Big)/\Delta t$, where $\Phi_{\Delta t}$ denotes the uncontrolled flow map and $\mathbf{O}(\mathbf{X})$ is constructed from the standardized state. For locally Lipschitz F, this rate equals $F(\mathbf{X}) + \mathcal{O}(\Delta t)$ as $\Delta t \to 0$, distinguishing finite-step bias from regression error. The corresponding one-step predictor is

$$\hat{\mathbf{X}}(t + \Delta t) = \mathbf{X}(t) + \Delta t\, \hat{F}(\mathbf{X}(t)). \tag{42}$$

Fitting Eq. (41) separately to the drive and response recordings yields $\hat{F}_d$ and $\hat{F}_r$. Autonomous forecasts are obtained by iterating Eq. (42).

The hyperparameters (q, ν) are selected separately for each system by Bayesian optimization using a Gaussian-process surrogate and the expected-improvement acquisition function [31], implemented in `scikit-optimize` [32]. Each search comprises 30 evaluations, including 8 initial random trials. Since map learning and control use one-step predictions, we optimize short-horizon accuracy rather than long-term autonomous forecasting. The objective is the standardized RMSE over N_s autonomous rollouts, each initialized at a measured evaluation state $\mathbf{X}(t_s)$ and advanced for N_p steps:

$$\text{RMSE} = \sqrt{\frac{1}{nN_sN_p}\sum_{s=1}^{N_s}\sum_{j=1}^{N_p}\Big\|\hat{\tilde{\mathbf{X}}}(t_s + j\Delta t) - \tilde{\mathbf{X}}(t_s + j\Delta t)\Big\|_2^2}, \tag{43}$$

where $N_p = 50$ spans one time unit and $N_s = 2000$, with 1000 initial times sampled randomly from each of the two evaluation recordings.

We restrict $q \le 3$ to obtain a compact feature basis that contains all polynomial terms of the HR vector fields. The switching term G is not represented exactly by this basis; moreover, the finite-time increment rates need not be cubic even for a cubic vector field. We search $\nu \in [10^{-10}, 1]$ on a logarithmic scale. Both searches select $q = 3$, yielding 35 drive features and 56 response features, including the constant term. On the test recordings, Eq. (43) gives RMSEs of 3.7×10^{-3} and 3.3×10^{-3} for the drive and response predictors, respectively. Figure 8 compares longer autonomous forecasts with the corresponding test trajectories.

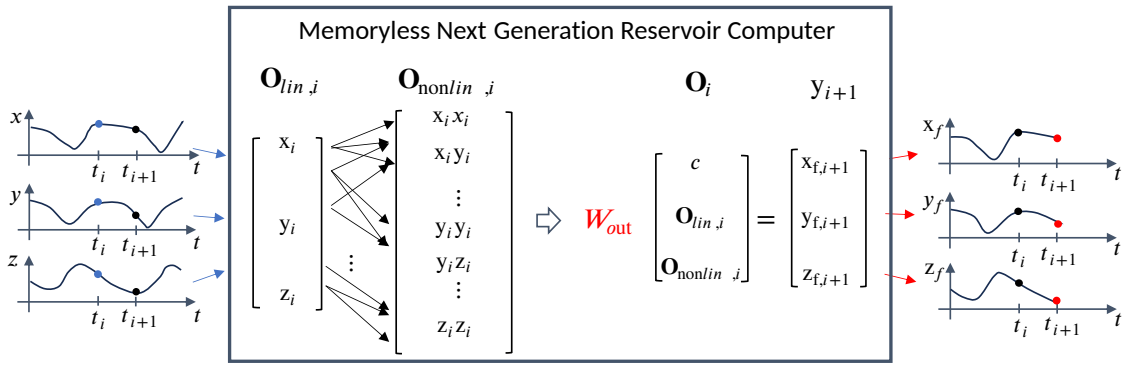

Figure 7 Schematic of memoryless NG-RC, adapted from [29]. The current state is represented by a feature vector comprising a constant, linear state components, and nonlinear monomials. A readout matrix W_{out}, fitted by ridge regression, maps these features to estimated state-increment rates, which determine the one-step prediction. No delayed states or recurrent reservoir are used.

6.2 Self-supervised learning of the synchronization map

We seek a map $\varphi_\theta : \mathbb{R}^4 \to \mathbb{R}^5$ whose graph is approximately invariant under the learned one-step dynamics, with the aim of reducing the control required to maintain $\mathbf{X}_r = \varphi_\theta(\mathbf{X}_d)$. The uncoupled recordings provide no paired drive–response targets for supervised regression. We therefore learn φ_θ through a self-supervised consistency objective: advancing a drive state with its learned predictor and then mapping should approximately agree with mapping first and advancing with the learned response predictor.

We parameterize φ_θ as an affine map in the standardized coordinates of Section 6.1. Let $\bar{\mathbf{X}}_d, \bar{\mathbf{X}}_r$ be the training means and $\mathbf{D}_d, \mathbf{D}_r$ the diagonal matrices of training standard deviations. With $\tilde{\mathbf{X}}_d = \mathbf{D}_d^{-1}(\mathbf{X}_d - \bar{\mathbf{X}}_d)$, we define

$$\varphi_\theta(\mathbf{X}_d) = \bar{\mathbf{X}}_r + \mathbf{D}_r\Big(\mathbf{A}\tilde{\mathbf{X}}_d + \mathbf{b}\Big), \tag{44}$$

where $\theta = (\mathbf{A}, \mathbf{b})$, $\mathbf{A} \in \mathbb{R}^{5\times 4}$, and $\mathbf{b} \in \mathbb{R}^5$, giving 25 trainable parameters. This family includes the reference correspondence $\varphi_{\theta_0}(\mathbf{X}_d) = (x, y, z, u, \bar{w}_r)^\top$, which matches the four shared variables and fixes the fifth at its response training mean $\bar{w}_r$. Standardization makes the entries of $\mathbf{A}$ dimensionless and comparable across components. Unlike the nonlinear map in Eq. (5), this family is affine and does not impose $\varphi_{\theta,4} = u$; hence, it does not preserve the specific memristive error structure used in Section 3.3.

We fit θ using N drive states $\mathbf{X}_{d,n}$ sampled from the drive training recordings. The two compositions of the map and the one-step predictors in Eq. (42) give

$$\begin{aligned}\mathbf{a}_n(\theta) &= \varphi_\theta\Big(\mathbf{X}_{d,n} + \Delta t\, \hat{F}_d(\mathbf{X}_{d,n})\Big),\\ \mathbf{b}_n(\theta) &= \varphi_\theta(\mathbf{X}_{d,n}) + \Delta t\, \hat{F}_r\Big(\varphi_\theta(\mathbf{X}_{d,n})\Big),\end{aligned} \tag{45}$$

where $\mathbf{a}_n$ advances then maps, whereas $\mathbf{b}_n$ maps then advances. Their agreement supplies a self-supervised training signal without paired response targets. We define the dynamics-consistency loss as

$$L_{\text{dyn}}(\theta) = \frac{1}{N}\sum_{n=1}^{N}\left\|\frac{\mathbf{a}_n(\theta) - \mathbf{b}_n(\theta)}{\Delta t}\right\|_2^2. \tag{46}$$

The consistency loss alone admits collapsed solutions: any constant map $\varphi_\theta \equiv \mathbf{c}$ satisfying $\hat{F}_r(\mathbf{c}) = \mathbf{0}$ yields $L_{\text{dyn}} = 0$ and ignores the drive. Such a solution targets an equilibrium of the learned response dynamics rather than a varying response to the drive. To discourage collapse, we introduce variance and covariance penalties inspired by VICReg [33], applied to the first four standardized target components. Let $\mathbf{A}_{1:4}$ contain the first four rows of $\mathbf{A}$, $\mathbf{C}_d$ be the sample covariance of the standardized training inputs $\tilde{\mathbf{X}}_{d,n}$, and $\mathbf{R}$ be the sample covariance of the first four standardized response components in the training recordings. The corresponding target covariance is $\mathbf{S}(\theta) = \mathbf{A}_{1:4}\mathbf{C}_d\mathbf{A}_{1:4}^\top$. We define

$$\begin{aligned}L_{\text{var}}(\theta) &= \sum_{i=1}^{4}\max\left(0,\, 1 - \sqrt{S_{ii}(\theta)}\right)^2,\\ L_{\text{cov}}(\theta) &= \sum_{\substack{i,j=1\\ i\neq j}}^{4}\Big(S_{ij}(\theta) - R_{ij}\Big)^2.\end{aligned} \tag{47}$$

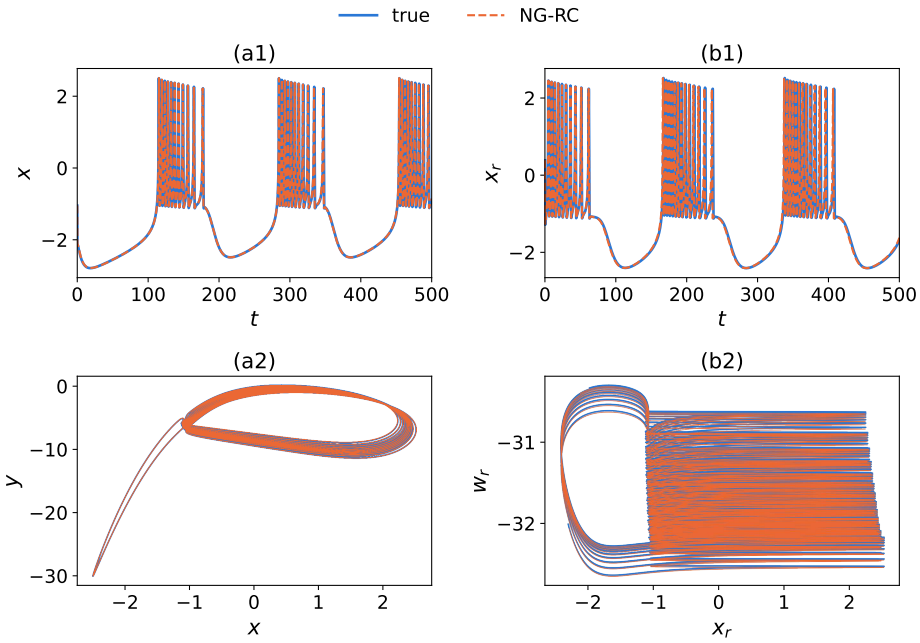

Figure 8 Autonomous NG-RC forecasts compared with test trajectories for (a) the drive and (b) the response: (a1, b1) membrane potentials; (a2, b2) phase-space projections for $t \geq 300$.

The variance penalty discourages target standard deviations below the unit scale of the standardized response data, while the covariance penalty discourages discrepancies in their off-diagonal covariances. Unlike VICReg, which penalizes off-diagonal covariances toward zero, we retain the dependence structure observed in the response recordings. These soft penalties do not prescribe a coordinate correspondence or guarantee a nondegenerate map. The fifth target is exempt from both penalties, allowing its variability to adjust to the slow w_r dynamics without imposing the variance of the uncontrolled response. Its dynamical compatibility remains enforced through L_{dyn}. The total training objective is

$$L(\theta) = L_{\mathrm{dyn}}(\theta) + \lambda_{\mathrm{var}} L_{\mathrm{var}}(\theta) + \lambda_{\mathrm{cov}} L_{\mathrm{cov}}(\theta), \qquad (48)$$

with $\lambda_{\mathrm{var}} = \lambda_{\mathrm{cov}} = 1$.

We minimize Eq. (48) using $N = 14400$ drive states, with 1800 sampled randomly from each of the eight training recordings. Optimization uses L-BFGS-B [34], implemented in `SciPy` [28], without parameter bounds. The initialization $\mathbf{A} = \mathbf{0}$, $\mathbf{b} = \mathbf{0}$ maps every drive state to the response training mean $\bar{\mathbf{X}}_r$, imposing no coordinate correspondence. In the implementation, $\sqrt{S_{ii}(\theta)}$ in Eq. (47) is evaluated as $\sqrt{S_{ii}(\theta) + \epsilon}$ with $\epsilon = 10^{-12}$, which makes L differentiable at the initialization, and its exact gradient is supplied to the optimizer. The stopping tolerances are 10^{-10} for the relative objective reduction and 10^{-7} for the infinity norm of the supplied gradient.

The objective decreases from 75.6 to 8.3×10^{-3} over 763 iterations (Figure 9). At the final iterate, $L_{\mathrm{dyn}} = 4.2 \times 10^{-3}$ on the training states and 3.2×10^{-3} on the evaluation states. As an independent consistency check, we replace both learned one-step predictors in Eq. (45) with fourth-order Runge–Kutta (RK4) steps of the uncoupled governing equations. Evaluated on the same training states, this diagnostic gives $L_{\mathrm{dyn}} = 3.3 \times 10^{-3}$ at the learned parameters (dashed curve in Figure 9). This comparable residual supports consistency with the underlying dynamics on the sampled states, although it does not exclude predictor errors elsewhere.

Without a prescribed coordinate correspondence, the learned linear part approximates that of the reference map φ_{θ_0}. The matrix $\mathbf{A}_{1:4}$ is nearly diagonal: its diagonal entries lie in $[0.98, 1.01]$ and differ from the corresponding reference entries by at most 0.04, while its off-diagonal entries have magnitude below 0.1. Its singular values lie in $[0.95, 1.05]$, indicating a well-conditioned mapping of the four standardized drive coordinates. The offsets differ from the reference values, most notably in the z_r component, whose target exceeds z by 0.63 at the mean drive state. The fifth

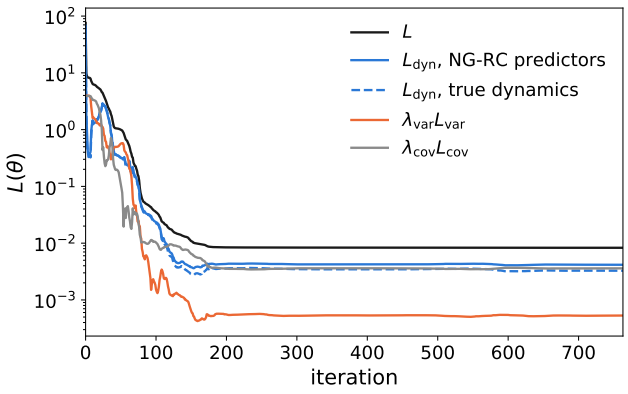

Figure 9 Training objective L in Eq. (48) and its weighted components during L-BFGS-B optimization. The dashed curve shows L_{dyn} evaluated using RK4 steps of the governing equations.

row is dominated by a coefficient of 0.027 on $\tilde{z}$, yielding a weakly varying w_r target consistent with its slow dynamics.

6.3 Data-driven coupling law

For the learned map, we define the synchronization error analogously to Eq. (6) as $\mathbf{e}_\theta(t) = \mathbf{X}_r(t) - \varphi_\theta(\mathbf{X}_d(t))$. The response is actuated through all five channels of Eq. (3). Inputs are updated at sampling times and applied through a zero-order hold: $\mathbf{v}(t') = \mathbf{v}(t)$ for $t' \in [t, t + \Delta t)$.

We construct a sampled-data analogue of Eq. (14) using learned predictors, following the NG-RC control approach of [22] and the discrete-time neural-network control framework of [35]. Let $\hat{\mathbf{X}}_d(t + \Delta t) = \mathbf{X}_d(t) + \Delta t\, \hat{F}_d(\mathbf{X}_d(t))$ and $\hat{\mathbf{X}}_r^{\text{free}}(t+\Delta t) = \mathbf{X}_r(t) + \Delta t\, \hat{F}_r(\mathbf{X}_r(t))$ denote the uncoupled one-step predictions. Approximating the effect of the held input to first order gives the controlled predictor $\hat{\mathbf{X}}_r^{\text{free}}(t + \Delta t) + \Delta t\, \mathbf{v}(t)$. Requiring its synchronization error to equal $\zeta\, \mathbf{e}_\theta(t)$, where $\zeta = e^{-\kappa \Delta t} \in (0, 1)$ and $\kappa > 0$, yields

$$\mathbf{v}(t) = \frac{\varphi_\theta\Big(\hat{\mathbf{X}}_d(t + \Delta t)\Big) - \hat{\mathbf{X}}_r^{\text{free}}(t + \Delta t) + \zeta\, \mathbf{e}_\theta(t)}{\Delta t}. \tag{49}$$

This contraction is imposed on the predictor; prediction errors and the approximate treatment of the held input prevent it from being an exact identity for the physical systems.

Substituting $\mathbf{X}_r(t) = \varphi_\theta(\mathbf{X}_d(t)) + \mathbf{e}_\theta(t)$ into Eq. (49) gives

$$\mathbf{v}(t) = \frac{\varphi_\theta\Big(\hat{\mathbf{X}}_d(t + \Delta t)\Big) - \varphi_\theta(\mathbf{X}_d(t))}{\Delta t} - \hat{F}_r(\mathbf{X}_r(t)) - \frac{1 - \zeta}{\Delta t}\, \mathbf{e}_\theta(t). \tag{50}$$

The three terms provide target-rate prediction, response-drift compensation, and proportional error feedback, respectively, paralleling Eq. (14). The effective feedback gain $(1 - \zeta)/\Delta t$ tends to κ as $\Delta t \to 0$. Unlike the analytical controller, this law treats the memristive channel identically to the others: its dynamics are approximately compensated through the learned predictors rather than retaining an explicit switching difference $G(u_r) - G(u)$. The response parameters remain fixed, and no adaptive parameter laws are used.

For numerical assessment, the governing equations represent the physical drive and response, while the controller accesses only sampled states. Unlike [8], where synchronization is imposed between two reservoir observers, the input acts directly on the response system. Both systems evolve uncoupled until $t = 100$, when control is activated with $\kappa = 1$. Between sampling times, we integrate both systems using RK4 with four substeps of size $\Delta t/4$, holding the response input constant. Figure 10 shows a representative trajectory: all five response components approach their targets within a few time units and subsequently track the mapped drive dynamics with small residual errors.

The errors in Figure 11 initially decay approximately at the prescribed rate $e^{-\kappa(t-100)}$. From $t \approx 105$, the error norm fluctuates between approximately 10^{-3} and 10^{-2}. We quantify tracking accuracy by the time average of $\|\mathbf{D}_r^{-1}\mathbf{e}_\theta(t)\|_2/\sqrt{5}$ and control effort by the temporal RMS of $\|\mathbf{D}_r^{-1}\mathbf{v}(t)\|_2$, both evaluated over the final fifty time units. Across eight initial-condition pairs, the median tracking error and control effort are 1.4×10^{-3} and 2.1×10^{-2}, respectively. Using the reference map φ_{θ_0} increases these values to 4.8×10^{-3} and 1.7×10^{-1}. Thus, the learned map reduces median control effort by a factor of approximately eight while improving tracking accuracy. Replacing both learned predictors with RK4 steps of the governing equations reduces the median error to 2.3×10^{-4}, indicating a substantial contribution from predictor inaccuracies. The remaining discrepancy is consistent with the approximate sampled-data control model and numerical

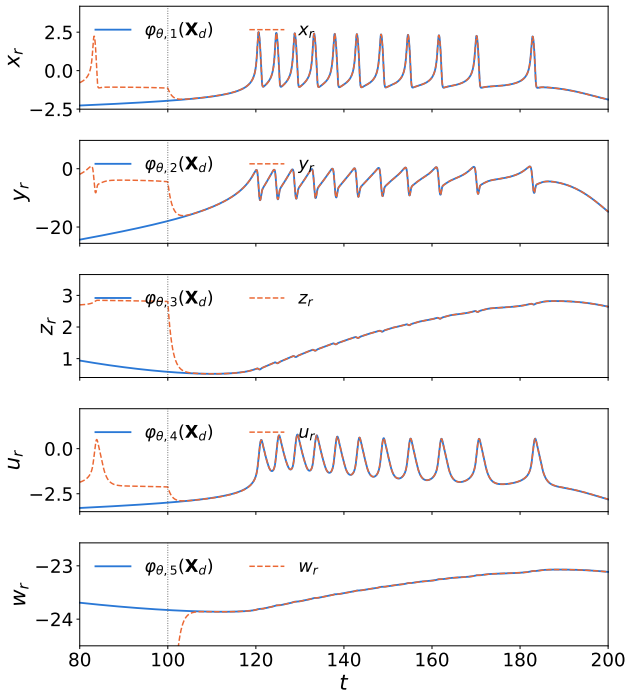

Figure 10 Response components and learned targets $\varphi_{\theta,i}(\mathbf{X}_d)$ under data-driven control. The black vertical dotted line marks control activation at $t = 100$.

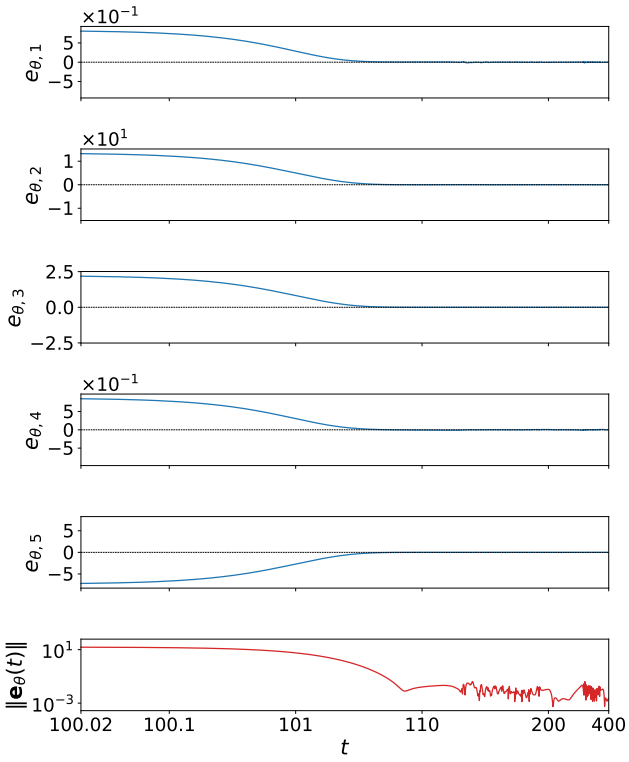

Figure 11 Synchronization error components and their Euclidean norm under data-driven control, shown after activation at $t = 100$ on logarithmic time axes.

integration; exact synchronization is not established by these experiments.

7 Summary and conclusion

We have investigated increased-order generalized synchronization (IOGS) between a four-dimensional memristive Hindmarsh–Rose drive and a five-dimensional response containing an additional slow adaptation variable. The dimensional mismatch makes the specification of a synchronization relationship an integral part of the control problem: the target map must assign a dynamical correspondence to every response component, including the variable without a counterpart in the drive. We addressed this problem through two complementary constructions, one based on a prescribed nonlinear map and adaptive Lyapunov design, and the other on an affine map learned from the consistency of data-driven predictors. These constructions connect the choice of synchronization manifold to two distinct objectives: retaining an error structure amenable to stability analysis and reducing the dynamical mismatch that the control must compensate.

In the analytical formulation, the constraint $\varphi_4 = u$ preserves the memristive switching difference explicitly in the closed-loop error dynamics. The adaptive laws cancel the parameter-error cross terms in the derivative of a quadratic Lyapunov function, while a case-wise analysis characterizes the remaining memristive contribution. Under the bounded-drive and global-existence assumptions of theorem 4.1, uniform strict dissipativity of this contribution yields asymptotic convergence of the synchronization error and boundedness of the parameter-estimation errors. Without the strict dissipativity condition, theorem 4.2 provides a switching-independent estimate of the form $\dot{V} \leq -\alpha\|e\|^2 + C$, identifying an explicit radius $\delta = \sqrt{C/\alpha}$ outside which V decreases. This radius characterizes a Lyapunov decrease threshold; the estimate does not, by itself, establish ultimate boundedness or practical synchronization in the asymptotic sense.

The numerical results delineate the distinction between these sufficient conditions and the observed dynamics. For the investigated trajectory at $m = 0.5$, the memristive contribution is nonpositive but vanishes

during visits to the central switching region $\mathcal{C}_5$, even when the corresponding error is nonzero. The uniform strict dissipativity hypothesis is therefore not satisfied, although all synchronization-error components decay toward zero over the simulated interval. The simulations thus indicate convergence beyond the conditions covered by the asymptotic theorem. Accurate recovery of the nominal parameters is also observed, but a general parameter-identification result would require additional excitation conditions that have not been established here.

The data-driven formulation addresses the same dimensional mismatch without supplying the governing equations to the learning or control algorithms. Memoryless next generation reservoir computing predictors are trained on uncoupled full-state recordings, and an affine synchronization map is learned by promoting agreement between mapping and one-step dynamical evolution. Variance and covariance penalties discourage collapsed target relationships without prescribing a coordinate correspondence. The resulting map approximately recovers the linear part of the reference correspondence while adjusting the offsets and the target associated with the additional response variable. A sampled-data feedback law constructed from the learned predictors then drives the response toward this target relationship, with the response parameters held fixed.

Across the eight initial-condition pairs considered, the learned map reduces the median control effort by approximately a factor of eight relative to the reference map within the same data-driven framework, while also reducing the median tracking error. These findings support the use of dynamical consistency as a criterion for selecting synchronization targets that require less corrective forcing. The remaining tracking error reflects limitations of both the learned predictors and the approximate sampled-data control model. Replacing the predictors with numerical flow maps obtained from the governing equations substantially reduces the residual, demonstrating a significant contribution from prediction error. The observed tracking performance nevertheless remains a numerical result rather than a proof of asymptotic synchronization or closed-loop stability.

The two approaches establish complementary roles for synchronization-map design. The analytical construction retains the memristive error structure and yields conditional convergence guarantees, whereas the learned construction seeks compatibility with the uncoupled dynamics and demonstrates reduced control effort. Their assumptions and target maps differ, so the numerical results do not constitute a direct performance comparison between the analytical and data-driven controllers. In particular, the data-driven implementation assumes full-state measurements and additive actuation of all response components, and its unconstrained affine map does not enforce the memristive-coordinate identity used in the analytical proof.

Several mathematical questions follow naturally from these results. A convergence analysis based on dissipation accumulated along trajectories could potentially weaken the uniform strict dissipativity requirement and account for the observed synchronization during intermittent visits to $\mathcal{C}_5$. For the data-driven scheme, stability estimates incorporating predictor errors and finite sampling would clarify how model accuracy and sampling rate determine the attainable tracking precision. Combining learned synchronization maps with explicit structural constraints offers a further direction for relating dynamical compatibility to rigorous convergence conditions. Extensions to partial observations and restricted actuation would subsequently help determine how these constructions perform under more limited access to the neuronal states.

Acknowledgements. We thank the Erlangen National High Performance Computing Center (NHR@FAU) for providing the computational resources used in this work.

Funding. This work was funded by the Department of Data Science (DDS), Friedrich-Alexander-Universität Erlangen-Nürnberg, Germany, and the Deutsche Forschungsgemeinschaft (DFG, German Research Foundation) via the grant YA 764/1-1 to M.E.Y—Project No. 456989199.

Data availability. The code supporting the findings of this study is publicly available at https://github.com/dennismstfc/iogs-analytical-vs-ml. All data and figures can be regenerated with the scripts provided there.

Declarations

Competing interests. The authors have no relevant financial or non-financial interests to disclose.

Appendix A Offline learning and online control for IOGS

Algorithm 1 summarizes the offline learning and online control stages described in Sections 6.1–6.3. Entire recordings are assigned to disjoint training, evaluation, and test sets; test data are reserved for final assessment. Each predictor search uses 30 trials, including 8 initial random proposals. Map optimization uses L-BFGS-B without parameter bounds, with the exact gradient, relative objective-reduction tolerance 10^{-10}, and gradient infinity-norm tolerance 10^{-7}. The variance penalty is smoothed as specified in Section 6.2. Control is activated at $t_{\mathrm{on}} = 100$ in the reported experiments.

Algorithm 1: Offline learning and online sampled-data control for IOGS

Input: Uncoupled training and evaluation recordings sampled at Δt; search ranges for (q, ν); map sample size N; weights $\lambda_{\mathrm{var}}, \lambda_{\mathrm{cov}}$; feedback rate $\kappa > 0$; activation time t_{on}.

Output: One-step predictors P_d, P_r; affine synchronization map φ_θ; applied control sequence $\mathbf{v}(t)$.

// Stage 1: learn the uncoupled predictors

foreach $s \in \{d, r\}$ **do**
- Compute training mean $\bar{\mathbf{X}}_s$ and scaling $\mathbf{D}_s$; standardize training and evaluation data using these statistics
- **for** $j \leftarrow 1$ **to** 30 **do**
  - Propose (q_j, ν_j) randomly for $j \le 8$, otherwise by Bayesian optimization
  - Construct features and increment-rate targets; fit $\mathbf{W}_j$ using Eqs. (40) and (41)
  - Evaluate rollout error J_j on evaluation recordings using Eq. (43)
- Retain $(q_j, \mathbf{W}_j)$ with the smallest J_j and define the corresponding increment-rate model $\hat{F}_s$
- $P_s(\mathbf{X}) \leftarrow \mathbf{X} + \Delta t\, \hat{F}_s(\mathbf{X})$

// Stage 2: learn the synchronization map

Sample N drive training states; compute their standardized covariance $\mathbf{C}_d$ and the covariance $\mathbf{R}$ of the first four standardized response training components

Initialize $\theta = (\mathbf{A}, \mathbf{b}) \leftarrow (\mathbf{0}, \mathbf{0})$

With P_d and P_r fixed, optimize $L(\theta)$ in Eq. (48) by L-BFGS-B, using the two-path residuals in Eq. (45) and the stated stopping criteria

// Stage 3: control the response online

$\zeta \leftarrow \exp(-\kappa \Delta t)$

foreach *sampling time* t **do**
- $\mathbf{v}(t) \leftarrow \mathbf{0}$
- **if** $t \ge t_{\mathrm{on}}$ **then**
  - Measure $\mathbf{X}_d(t)$ and $\mathbf{X}_r(t)$
  - $\mathbf{e} \leftarrow \mathbf{X}_r(t) - \varphi_\theta(\mathbf{X}_d(t))$
  - $\mathbf{v}(t) \leftarrow \left[\varphi_\theta(P_d(\mathbf{X}_d(t))) - P_r(\mathbf{X}_r(t)) + \zeta \mathbf{e}\right] / \Delta t$
- Hold $\mathbf{v}(t)$ constant on $[t, t + \Delta t)$ and apply it additively to the response

References

[1] G. Buzsáki, Rhythms of the Brain, Oxford University Press, 2006. doi:10.1093/acprof:oso/9780195301069.001.0001.

[2] K. Lehnertz, S. Bialonski, M.-T. Horstmann, D. Krug, A. Rothkegel, M. Staniek, T. Wagner, Synchronization phenomena in human epileptic brain networks, Journal of Neuroscience Methods 183 (1) (2009) 42–48. doi:10.1016/j.jneumeth.2009.05.015.

[3] L. M. Pecora, T. L. Carroll, Synchronization in chaotic systems, Physical Review Letters 64 (8) (1990) 821. doi:10.1103/PhysRevLett.64.821.

[4] E. M. Yamakou, E. M. Inack, F. Moukam Kakmeni, Ratcheting and energetic aspects of synchronization in coupled bursting neurons, Nonlinear Dynamics 83 (1) (2016) 541–554. doi:10.1007/s11071-015-2346-0.

[5] N. F. Rulkov, M. M. Sushchik, L. S. Tsimring, H. D. I. Abarbanel, Generalized synchronization of chaos in directionally coupled chaotic systems, Physical Review E 51 (2) (1995) 980–994. doi:10.1103/PhysRevE.51.980.

[6] L. Kocarev, U. Parlitz, Generalized synchronization, predictability, and equivalence of unidirectionally coupled dynamical systems, Physical Review Letters 76 (11) (1996) 1816–1819. doi:10.1103/PhysRevLett.76.1816.

[7] R. Femat, G. Solís-Perales, Synchronization of chaotic systems with different order, Physical Review E 65 (3) (2002) 036226. doi:10.1103/PhysRevE.65.036226.

[8] J. Kobiolka, J. Habermann, M. E. Yamakou, Reduced-order adaptive synchronization in a chaotic neural network with parameter mismatch: a dynamical system versus machine learning approach, Nonlinear Dynamics 113 (10) (2025) 10989–11008. doi:10.1007/s11071-024-10821-6.

[9] S. Ogunjo, Increased and reduced order synchronization of 2D and 3D dynamical systems, International Journal of Nonlinear Science 16 (2) (2013) 105–112.

[10] K. S. Ojo, S. T. Ogunjo, A. N. Njah, I. A. Fuwape, Increased-order generalized synchronization of chaotic and hyperchaotic systems, Pramana - Journal of Physics 84 (1) (2015) 33–45. doi:10.1007/s12043-014-0835-1.

[11] Q.-Y. Miao, J.-A. Fang, Y. Tang, A.-H. Dong, Increasing-order projective synchronization of chaotic systems with time delay, Chinese Physics Letters 26 (5) (2009) 050501. doi:10.1088/0256-307X/26/5/050501.

[12] J. L. Hindmarsh, R. M. Rose, A model of neuronal bursting using three coupled first order differential equations, Proceedings of the Royal Society of London. Series B. Biological Sciences 221 (1222) (1984) 87–102. doi:10.1098/rspb.1984.0024.

[13] J. Zhang, Z. Li, Switchable memristor-based Hindmarsh–Rose neuron under electromagnetic radiation, Nonlinear Dynamics 112 (8) (2024) 6647–6662. doi:10.1007/s11071-024-09399-w.

[14] M. E. Yamakou, Chaotic synchronization of memristive neurons: Lyapunov function versus Hamilton function, Nonlinear Dynamics 101 (1) (2020) 487–500. doi:10.1007/s11071-020-05715-2.

[15] M. M. Al-sawalha, M. S. M. Noorani, Adaptive increasing-order synchronization and anti-synchronization of chaotic systems with uncertain parameters, Chinese Physics Letters 28 (11) (2011) 110507. doi:10.1088/0256-307X/28/11/110507.

[16] B. Babaeian, M. E. Yamakou, A lyapunov stability proof and a port-hamiltonian physics-informed neural network for chaotic synchronization in memristive neurons, Applied Mathematics and Computation 530 (2026) 130157. doi:10.1016/j.amc.2026.130157.

[17] D. Durstewitz, G. Koppe, M. I. Thurm, Reconstructing computational system dynamics from neural data with recurrent neural networks, Nature Reviews Neuroscience 24 (11) (2023) 693–710. doi:10.1038/s41583-023-00740-7.

[18] S. L. Brunton, J. N. Kutz, Data-Driven Science and Engineering: Machine Learning, Dynamical Systems, and Control, 2nd Edition, Cambridge University Press, 2022. doi:10.1017/9781009089517.

[19] T. Weng, H. Yang, C. Gu, J. Zhang, M. Small, Synchronization of chaotic systems and their machine-learning models, Physical Review E 99 (4) (2019) 042203. doi:10.1103/PhysRevE.99.042203.

[20] Z. Lu, J. Pathak, B. Hunt, M. Girvan, R. Brockett, E. Ott, Reservoir observers: Model-free inference of unmeasured variables in chaotic systems, Chaos: An Interdisciplinary Journal of Nonlinear Science 27 (4) (2017) 041102. doi:10.1063/1.4979665.

[21] A. Nazerian, C. Nathe, J. D. Hart, F. Sorrentino, Synchronizing chaos using reservoir computing, Chaos: An Interdisciplinary Journal of Nonlinear Science 33 (10) (2023) 103121. doi:10.1063/5.0161076.

[22] R. M. Kent, W. A. S. Barbosa, D. J. Gauthier, Controlling chaotic maps using next-generation reservoir computing, Chaos: An Interdisciplinary Journal of Nonlinear Science 34 (2) (2024) 023102. doi:10.1063/5.0165864.

[23] R. M. Kent, W. A. S. Barbosa, D. J. Gauthier, Controlling chaos using edge computing hardware, Nature Communications 15 (2024) 3886. doi:10.1038/s41467-024-48133-3.

[24] J. J. Bramburger, S. L. Brunton, J. N. Kutz, Deep learning of conjugate mappings, Physica D: Nonlinear Phenomena 427 (2021) 133008. doi:10.1016/j.physd.2021.133008.

[25] M. Falcke, R. Huerta, M. I. Rabinovich, H. D. Abarbanel, R. C. Elson, A. I. Selverston, Modeling observed chaotic oscillations in bursting neurons: the role of calcium dynamics and ip3, Biological Cybernetics 82 (6) (2000) 517–527. doi:10.1007/s004220050604.

[26] E. M. Ngouonkadi, H. Fotsin, P. L. Fotso, V. K. Tamba, H. A. Cerdeira, Bifurcations and multistability in the extended Hindmarsh–Rose neuronal oscillator, Chaos, Solitons & Fractals 85 (2016) 151–163. doi:10.1016/j.chaos.2016.02.001.

[27] J. R. Dormand, P. J. Prince, A family of embedded Runge-Kutta formulae, Journal of Computational and Applied Mathematics 6 (1) (1980) 19–26. doi:10.1016/0771-050X(80)90013-3.

[28] P. Virtanen, R. Gommers, T. E. Oliphant, M. Haberland, T. Reddy, D. Cournapeau, E. Burovski, P. Peterson, W. Weckesser, J. Bright, et al., SciPy 1.0: fundamental algorithms for scientific computing in Python, Nature Methods 17 (3) (2020) 261–272. doi:10.1038/s41592-019-0686-2.

[29] D. J. Gauthier, E. Bollt, A. Griffith, W. A. S. Barbosa, Next generation reservoir computing, Nature Communications 12 (1) (2021) 5564. doi:10.1038/s41467-021-25801-2.

[30] H. Jaeger, The "echo state" approach to analysing and training recurrent neural networks - with an Erratum note, GMD Report 148, German National Research Center for Information Technology GMD, Bonn, Germany (2001).

[31] J. Snoek, H. Larochelle, R. P. Adams, Practical Bayesian optimization of machine learning algorithms, in: Advances in Neural Information Processing Systems, Vol. 25, 2012, pp. 2951–2959. doi:10.48550/arXiv.1206.2944.

[32] T. Head, M. Kumar, H. Nahrstaedt, G. Louppe, I. Shcherbatyi, Scikit-optimize/scikit-optimize (2021). doi:10.5281/zenodo.6451894.

[33] A. Bardes, J. Ponce, Y. LeCun, VICReg: Variance-invariance-covariance regularization for self-supervised learning, International Conference on Learning Representations (ICLR) (2022). doi:10.48550/arXiv.2105.04906.

[34] R. H. Byrd, P. Lu, J. Nocedal, C. Zhu, A limited memory algorithm for bound constrained optimization, SIAM Journal on Scientific Computing 16 (5) (1995) 1190–1208. doi:10.1137/0916069.

[35] J. Sarangapani, Neural Network Control of Nonlinear Discrete-Time Systems, CRC Press, Boca Raton, 2006. doi:10.1201/9781420015454.